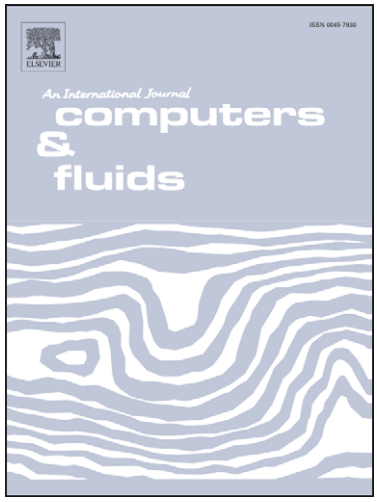

High-Order Implicit Large Eddy Simulation of Gaseous Fuel Injection and Mixing in a Combustor

Y. Shimada, B. Thornber, D. Drikakis

PII: S0045-7930(11)00012-0
DOI: 10.1016/j.compfluid.2011.01.005
Reference: CAF 1509

To appear in: *Computers & Fluids*

Received Date: 27 January 2010
Revised Date: 20 October 2010
Accepted Date: 6 January 2011

Please cite this article as: Shimada, Y., Thornber, B., Drikakis, D., High-Order Implicit Large Eddy Simulation of Gaseous Fuel Injection and Mixing in a Combustor, *Computers & Fluids* (2011), doi: 10.1016/j.compfluid.2011.01.005

Computers & Fluid, Volume 44, Issue 1, May 2011, Pages 229-237

High-Order Implicit Large Eddy Simulation of Gaseous Fuel Injection and Mixing of a Bluff Body Burner

Y. Shimada[a], B. Thornber[a], D. Drikakis[*,a]

[a] *Department of Fluid Mechanics and Computational Science, Cranfield University, Cranfield, Bedfordshire, MK43 0AL, UK*

Abstract

Implicit Large Eddy Simulation (ILES) with high-resolution and high-order computational modelling was applied to a turbulent mixing fuel injector flow. In the ILES calculation, the governing equations for three dimensional, non-reactive, multi-species compressible flows were solved using a finite volume Godunov-type method. Up to ninth-order spatial accurate reconstruction methods were examined with a second order explicit Runge-Kutta time integration. Mean and root mean square velocity and mixture fraction profiles showed good agreement with experimental data, which demonstrated that ILES using high-order methods successfully captured complex turbulent flow structure without using an explicit subgrid scale model. The effects of grid resolution and the influence of order of spatial accuracy on the resolution of the kinetic energy spectrum were investigated. An $k^{-5/3}$ decay of energy could be seen in a certain range and the cut-off wavenumbers increased with grid resolution or order of spatial accuracy. The effective cut-off wavenumbers are shown to be larger than the maximum wavenumbers appearing on the given grid for all test cases, implying that the numerical dissipation represents sufficiently the energy transport between resolved and unresolved eddies. The fifth-order limiter with a 0.6 million grid points was found to be optimal in terms of the resolution of kinetic energy and reasonable computational time.

Key words: Large eddy simulation, High-resolution, High-order, Turbulent mixing, Fuel injector

[*]Corresponding author. Tel: +44 1234 754796 Fax: +44 1234 758027.
Email address: d.drikakis@cranfield.ac.uk (D. Drikakis)

PACS: 47.27

1. Introduction

Fuel jet injection and mixing with air has a major impact on overall combustor performance and the flow field contains many complex fluid mechanical phenomena: transition of the fuel jet from laminar to turbulent, forming of the recirculation zones, vortex breakdown and turbulent mixing and hence, numerous experiments and computations have been conducted. In the context of numerical research, with the aid of recent developments in computational power, Large Eddy Simulation (LES) has been applied for these flows since LES has been recognised as a more promising approach for time dependent flows than the Reynolds Averaged Navier-Stokes Simulation approach in which only temporally averaged values are available.

In this decade, extensive research has been carried out on several specific configurations of reactive and non-reactive fuel jet flows in the framework of a series of the International Workshop on Measurement and Computation of Turbulent Nonpremixed Flames (TNF) which is summarised in [1, 2]. In this research, all of three dimensional non reactive computations used a conventional LES approach to deal with turbulence, and solved the filtered governing equations together with explicit turbulence models, e.g., a Smagorinsky's eddy viscosity model. Grid resolutions varied for each method from 1×10^6 to 4×10^6 grid points [1]. Though grid convergence was examined for a method up to 4.0×10^7 grid points [2] grid dependancy still can be seen near the central jet region. The sampling periods varied from $10ms$ to $30ms$, which are relatively short time compared to reactive test cases. The computational costs also varied from the order of $100hr$ to $1000hr$ depending on the grid resolutions and numerical methods. In a comparative work of two numerical methods [6], authors combined different chemical reaction models to fluid dynamics by the flamelet concept however, the turbulent subgrid scales were the same Smagorinsky model. Both methods applied second-order spatial discretisation. The inflow boundary condition is one of the key points for accurate simulation and hence, each simulation set them carefully; one applied upstream boundaries with turbulent generation and the other put random fluctuations. Other results of the TNF non reactive test cases can be found in, e.g., [3, 4].

These results showed a reasonable agreement with experimental data but at the same time showed some limitations. As described in [2], the simulation

is sensitive to the subgrid scale model coefficient which effects both velocity and scalar fields. Moreover, the constant turbulent Schmidt number often used in the conventional LES [5, 6] is involved in the subgrid scale model and this may cause the deviation in the scalar field. Therefore, to preset and tune up these coefficients can be a difficult task. A well known solution is to apply the dynamic procedure [7], which can avoid an explicit setting of the model coefficient, however, this results in strong dependence of the turbulent viscosity on grid resolution and, hence, the conventional LES requires sufficiently large grid size. In the conventional LES, the filtered equations are derived assuming the commutation between differentiated and filtered variables but this assumption is valid only with equal filter length, which is not likely in many cases of complex geometry. A number of other issues are reported in past reviews (see, for example, [8]). These problems are basically unavoidable as long as filtering is explicitly operated to the governing equations.

Implicit Large Eddy Simulation (ILES) techniques (see reviews [9, 10, 11]) together with high-resolution methods [12, 13] have been developed to overcome the principal disadvantages of the conventional LES approach described above. In ILES computation it is assumed that the numerical discretisation itself accounts for unresolved scales, in other words implicitly separates scales, and hence setting explicit filters for determination of subgrid scale is unnecessary. Furthermore, the use of appropriate limiters in the reconstruction process of high-resolution methods, which are employed in ILES, accomplishes non-linear dissipation to be selectively added to the computational cells. The numerical dissipation is a function of the eigenstructure of the non-linear (advective) terms of the Navier-Stokes equations and acts locally with the flow field depending on the flow gradients.

There are a number of recent and past studies, which have demonstrated the accuracy of ILES in simulations of both basic and complex flows, e.g., [9, 10, 32, 15, 16, 17, 18, 19, 20, 21, 22, 23, 24, 25, 26, 27, 28, 29], as well as studies dealing with theoretical aspects of ILES and their associated numerical methods [9, 10, 30, 31]. ILES methods have also been validated in the past with respect to gas turbine combustor flows [15, 16]. In [16] two LES models, a second-order ILES model with 1 and 2 step Arrhenius chemistry, and a fractal flame-wrinkling LES model coupled to a conventional one-equation eddy-viscosity subgrid model, were used. The authors showed reasonable agreement when comparing their predictions with experimental data and with other LES computations of the same case.

The aim of the present paper is assess the accuracy of higher-order ILES methods for non reactive, multi-species fuel jet flows. The paper is organised as follows. Section 2 presents the governing equations and the ILES models. Section 3 presents the test case geometry of a fuel jet injector and the numerical setup. The ILES results, including instantaneous and mean flow structures, mean velocity and mixture fraction profiles, and comparisons with the experimental data are presented in Section 4. Finally, Section 5 summarises the main conclusions drawn from the present study.

2. ILES Numerical Methods

2.1. Governing Equations

The three dimensional compressible flow mass, momentum and energy conservation laws for a gas mixture were employed. For multi-species modelling a quasi conservative model [33] was adopted. In this model the volume fraction of fuel is tracked and hence, the mixture mass conservation equation was replaced by a balance equation of volume fraction.

An instantaneous pressure equilibrium assumption was applied in which both species in the mixture have the same velocity and pressure within a single volume cell. Under these conditions the governing equations are,

$$\frac{\partial \alpha_f \rho_f}{\partial t} + \boldsymbol{\nabla} \cdot (\alpha_f \rho_f \boldsymbol{u}) = 0, \tag{1}$$

$$\frac{\partial \alpha_o \rho_o}{\partial t} + \boldsymbol{\nabla} \cdot (\alpha_o \rho_o \boldsymbol{u}) = 0, \tag{2}$$

$$\frac{\partial \rho \boldsymbol{u}}{\partial t} + \boldsymbol{\nabla} \cdot (\rho \boldsymbol{u}\boldsymbol{u}) = -\boldsymbol{\nabla} \cdot \boldsymbol{P}, \tag{3}$$

$$\frac{\partial \rho E}{\partial t} + \boldsymbol{\nabla} \cdot (\rho E \boldsymbol{u}) = -\boldsymbol{\nabla} \cdot (\boldsymbol{P} \cdot \boldsymbol{u}) - \boldsymbol{\nabla} \cdot \boldsymbol{q}, \tag{4}$$

$$\frac{\alpha_f}{\partial t} + \boldsymbol{\nabla} \alpha_f \cdot \boldsymbol{u} = 0, \tag{5}$$

$\boldsymbol{u}$ is the velocity vector, α, ρ and E denote respectively volume fraction, density of mixture and total energy per unit volume. where the subscript f and o designate species for fuel and oxidiser. Variables for mixture and each species are related by,

$$\alpha_f + \alpha_o = 1, \tag{6}$$

$$\rho = \rho_f \alpha_f + \rho_o \alpha_o, \tag{7}$$

and other thermodynamical parameters are specified in [33]. The total energy is a sum of internal energy and kinetic energy,

$$E = C_v T + \frac{1}{2} uu, \tag{8}$$

where C_v and T are the specific heat for constant volume of the mixture and temperature. The stress tensor $\boldsymbol{P}$ contains pressure and viscous effect based on Stoke's hypothesis,

$$\boldsymbol{P} = p\boldsymbol{I} + \frac{2}{3}\mu(\boldsymbol{\nabla} \cdot \boldsymbol{u})\boldsymbol{I} - \mu((\boldsymbol{\nabla u}) + (\boldsymbol{\nabla u})^T), \tag{9}$$

where p, $\boldsymbol{I}$, μ and $\boldsymbol{q}$ respectively stand for pressure, unit tensor, the dynamic viscosity coefficient and the heat flux following Fourier's law. The mixture specific heat ratio γ is evaluated by constant specific heat ratio for each species, and ideal gas equation of state can be used to relate pressure, temperature and specific heat ratio then, close the system,

$$p = \rho C_v T(\gamma - 1). \tag{10}$$

Regarding transport properties, viscosity coefficients are calculated by the Sutherland's law, and heat conductivity can be evaluated by a constant Prandtl number 0.72. In the current simulation diffusion terms are neglected from species and energy equations since usually they are much smaller than turbulent diffusion terms in the ILES algorithm. However, it should be noted that sensitivity of these transport properties can cause deviation in the multi-species flow simulation.

2.2. Numerical Scheme

The governing equations are solved using a finite volume Godunov-type method. In this method, the fluxes at the cell interfaces are reconstructed with a limiter, and therefore limiters control the order of the spatial accuracy.

To achieve high-order spatial accuracy, up to ninth-order accurate limiter were used in the simulations. The Monotonic Upstream-centred Scheme for Conservation Laws (MUSCL) limiters were used for a second-order [34] and a

fifth-order [35] accurate scheme and the Weighted Essentially Non-Oscillatory (WENO) scheme was used for a ninth-order scheme [36].

In the reconstruction process, the velocity components are locally modified according to a procedure detailed in [31] to prevent overly dissipative behaviour of turbulent kinetic energy, particularly in low Mach number flow. This is because the leading order dissipation rate was found to be proportional to the speed of sound and hence, caused excessive dissipation in low Mach number flow [31]. With this modification under subsonic conditions, the leading order of the truncation errors which act as subgrid stresses in the ILES approach, for second, fifth and ninth-order limiters applied in the current paper are given by [32, 31, 37],

$$\varepsilon^{2ndMUSCL} = \frac{\Delta x^2}{12} u u^{(1)} u^{(2)} + \frac{\Delta x^3}{12} C a u^{(1)} u^{(3)} \ , \tag{11}$$

$$\varepsilon^{5thMUSCL} = \frac{\Delta x^5}{60} u u^{(1)} u^{(5)} \ , \tag{12}$$

$$\varepsilon^{9thWENO} = \frac{\Delta x^9}{1260} u u^{(1)} u^{(9)} \ , \tag{13}$$

where Δx, a, u and C denote grid spacing, speed of sound, velocity in direction normal to the cell interface and the Courant-Friedrich-Levy (CFL) number, respectively, the superscript (n) denotes the n-th derivative with respect to the cell interface normal. It should be noted that in the second-order reconstruction scheme the dissipation rate still includes the speed of sound.

As an approximate Riemann solver, the Harten Lax and van Leer Riemann solver plus contact wave (HLLC) method [13] was applied. The viscous term was discretised using standard central differences. For time integration, a second-order explicit Runge-Kutta method was employed.

In the ILES computation stated above, the discretisation to cell centred values and the reconstruction by a limiter are the main feature to obtain high-order accuracy. Therefore, grid resolution and order of reconstruction limiters are the key parameters for accurate ILES computation.

3. Test Case Description

3.1. Experimental Data

The test case is the Sydney bluff body burner shown in Figure 1. The flow was investigated experimentally by Dally et.al. [38] and the data is available on the Sydney University website [39]. Compressed natural gas (mainly composed of methane) and air were used in the experiments. Due to its simple and generic geometry but complex flow structure, this injector is suitable for validation of LES methodologies. The injector consists of a fuel jet nozzle, a bluff body and an annulus oxidiser flow inlet. Fuel is injected in the axial direction through the round exit nozzle (diameter $3.6mm$) located in the centre of a cylindrical bluff body (diameter $50.0mm$). The oxidiser is supplied in the axial direction from the annulus inlet (width $5.0mm$) surrounding the bluff body. The jet injector is located in the centre of a wind tunnel which supplies constant air flow as coflow surrounding the injector. The flow field is entirely controlled by the three inflows, namely the fuel inlet velocity, the oxidiser inlet velocity and the coflow velocity.

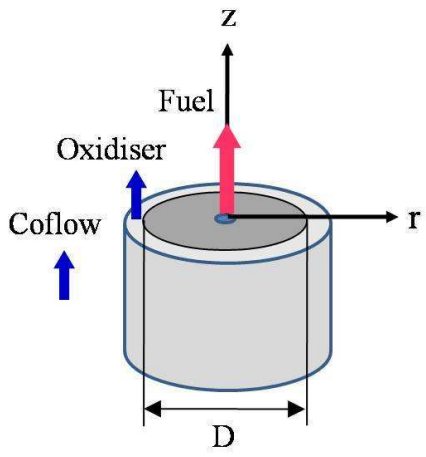

Figure 1: Schematic view of the jet flow

3.2. Numerical Setup

The computational domain is cylindrical; the axial and radial lengths are $5.0D$ and $8.8D$ respectively, where D is the diameter of the bluff body. The size was similar to one employed by [5] which has a smaller axial length,

3.0D. To investigate effects of grid resolution and order of reconstruction limiters the computations were carried out with four grid resolutions and three limiters. In the study of flow structure and comparison of velocity profile, air was selected for both fuel and oxidiser, corresponding to the experimental study [39]. For evaluation of multi-species mixing flow, methane and air were selected as fuel and oxidiser, respectively. The mean bulk inlet velocity conditions are $61m/s$ for air jet and $85m/s$ for methane jet, and $20m/s$ for the oxidiser and coflow, respectively. The Reynolds number based on the fuel inlet velocity and the fuel nozzle diameter is 1.45×10^4. The local Mach number based on the fuel inlet velocity is 0.18 for air jet case and 0.14 for methane jet case. Test cases are summarised in Table 1 with N_z,N_r, N_c and N_t being the axial, radial, circumferential and total cell numbers, respectively.

Grid	N_z	N_r	N_c	N_t	limiter	Jet
Coarse	60	62	32	0.12×10^6	5th MUSCL	Air
Medium	300	62	32	0.60×10^6	2nd MUSCL	Air
Medium	300	62	32	0.60×10^6	5th MUSCL	Air
Medium	300	62	32	0.60×10^6	5th WENO	Methane
Medium	300	62	32	0.60×10^6	9th WENO	Air
MediumCirc	300	64	64	1.23×10^6	5th MUSCL	Air
Fine	600	124	32	2.38×10^6	5th MUSCL	Air
reference LES [5]	300[a]	60	32	0.58×10^6	-	Air

[a] the axial length is $3D$

Table 1: Test cases

Turbulent velocity fluctuations were added to the fuel and the oxidiser inflows based on a Direct Numerical Simulation result [40], but the turbulent intensity profile was simplified as linear from the wall of the nozzle and inlet though the reference paper showed nonlinear profiles. The inflow velocity matches the Reynolds stresses in the DNS however spectral data and correlations are not reproduced. The inflow gas temperature and static pressure of both species are at standard atmospheric temperature and pressure. No slip condition was applied for the bluff body plate. On the radial boundary only constant axial velocity component and species corresponding to coflow were set. The downstream plain of the domain was set as outflow boundary where velocity and species gradients were zero.

4. Results and Discussion

This section will first show the instantaneous flow visualisations to illustrate the turbulent flow structure. Next, temporally and spatially averaged velocity, root mean square (rms) velocity and mixture fraction profiles are compared with experimental data. The comparisons of the ILES results with the experiment are presented using the fifth-order reconstruction limiter, which offered the best overall performance with respect to accuracy and computational cost. Following these comparisons, we will then discuss the kinetic energy spectra to assess effects of grid resolution and order of reconstruction limiters in the ILES computation.

4.1. Instantaneous and Mean Flow Structure

The instantaneous flow field was examined to deduce the structure of the large scale eddies. Figure 2(left) shows fuel volume fraction contour flood of the fully turbulent flow field. The simulation was performed on the fine grid with the fifth-order accurate limiter. The corresponding physical time from fuel injection is $163.9\,ms$. Note that air was applied as fuel jet species in this test case as described in Table 1. In the figure the central fuel jet is laminar at $z/D < 0.4$. The jet then breaks up immediately and a highly turbulent region can be observed at $0.4 < z/D < 1.0$ where the fuel volume fraction is reduced to less than 0.5. A low fuel volume can be seen in the recirculation region ($-0.5 < r/D < 0.5$, $0.0 < z/D < 1.0$). Normalised vorticity magnitude at the same instant is shown in Figure 2 (right). A high vorticity region where mixing of the fuel and air is enhanced exists only in the vicinity of the central fuel jet and $0.0 < z/D < 1.0$.

Figure 3 (left) shows a contour flood of the temporally averaged axial velocity. The velocity is normalised by U_0; the mean fuel inlet velocity at the centre ($r/D = 0.0$). With a long physical sampling time $114.8\,ms$, which corresponds to more than nine times passage of the coflow through the computational domain, axially symmetric axial velocity was obtained. It clearly depicts the location of recirculation zones where the axial velocity is negative, i.e., in $0.1 < |r/D| < 0.4$, $z/D < 1.0$. Figure 3 (right) shows the contour of the temporally averaged axial rms velocity of the same flow. A high rms velocity region where turbulent intensity is high lies mainly on the centreline at around $z/D = 0.4$. Although the sampling time is very long, still small asymmetry can be seen in this region.

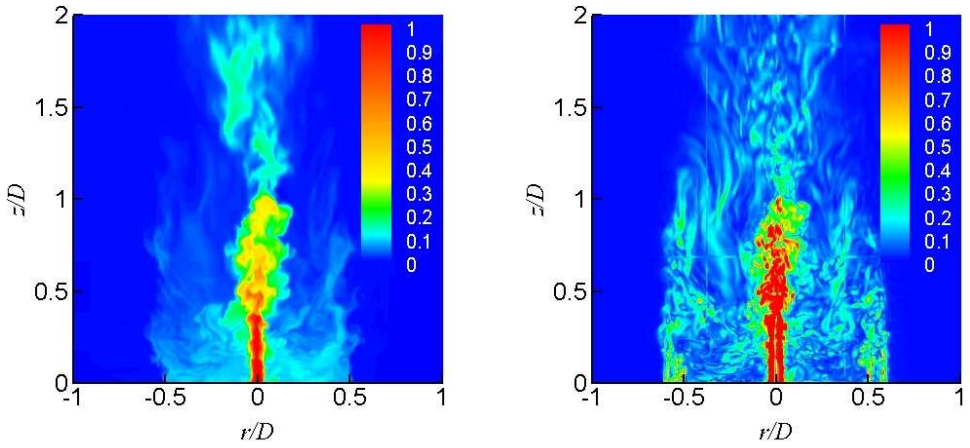

Figure 2: Instantaneous snapshot of volume fraction (left) and vorticity magnitude (right) (fifth-order limiter, fine grid)

4.2. Velocity Field

The comparisons of the mean flow with experimental data [39] were performed at $z/D = 0.4$, 0.8 and 1.4, corresponding to a location of the strong turbulence and the centre of the recirculation zone, the top boundary of the recirculation zone, and the downstream region, respectively. Note that the experimental data consists of three sets of measurement. Also, LES results by [5], employing Smagorinsky model as an explicit subgrid scale modelling, are plotted allowing comparison to a representative state-of-the-art conventional LES result. Although the flow field in Figure 3 left is almost axially symmetric, circumferential averaging of the flow is applied to take into account the spatial variance of the flow structure, e.g., shown in Figure 2.

Figure 4 shows mean axial velocity and axial rms velocity. The sampling time began at $49.2\,ms$ from fuel jet injection and the sampling period was $114.8\,ms$. In general, the ILES results well match to the experimental data in all axial locations. At $z/D = 0.8$ and 1.4, a velocity deviation from the experimental data can be seen at the centreline $r/D = 0.0$ where the velocity gradient is very large and a small axial difference causes a large velocity deviation. Also, a large rms velocity at $(r/D, z/D) = (0.0, 0.4)$ implies that the added inflow boundary fluctuation velocity is larger than the experimental data and hence, reduces the axial velocity more rapidly causing the deviation of the axial velocity at the centreline. As pointed out previously

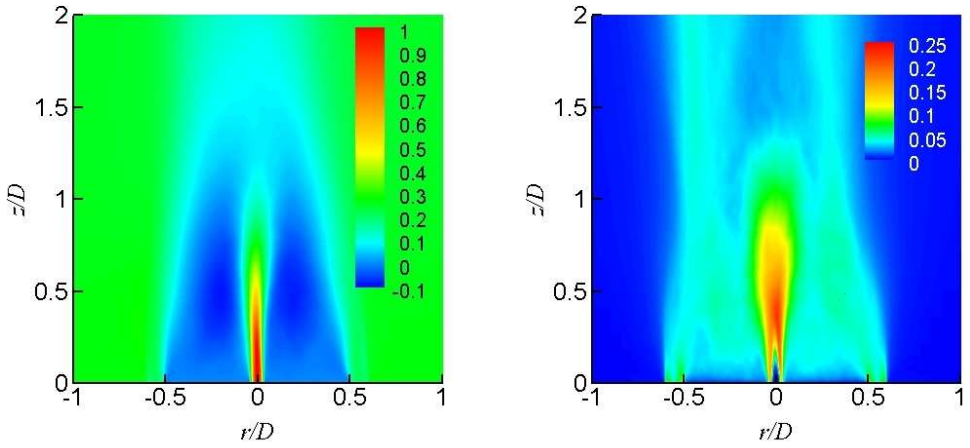

Figure 3: Temporally averaged axial velocity (left) and axial rms velocity (right) (fifth-order limiter, fine grid)

(e.g., [5]), the flow profiles are very sensitive to the form of turbulent inlet conditions; a detailed setup of the inflow velocity fluctuations as the same as the experimental conditions (spectra and correlations) should result in a better match to the experimental measurements. The radial locations of zero axial velocity are useful information since they can indicate the centre axis of the recirculation zones and the ILES results predict them precisely.

Figure 5 shows mean radial velocity and radial rms velocity. Again, in general, the ILES results show good agreement with experimental data. Although deviation can be observed particularly in near central fuel jet region, it should be noted that the vertical axis range of the graph is small in this figure and the velocity level is small compared to the axial velocities. The experimental data shows a large variance of mean velocity at $z/D = 0.8$ and rms at $z/D = 0.4$ and 0.8, where rms velocity level is higher than the mean values. In these regions simulations also show some deviations from the experimental data, which implies that the radial velocity and its rms of these regions are sensitive to the inflow conditions, most notably the inflow fluctuations. The radial locations of zero radial velocity in this graph indicate that the boundary of the recirculation zones and the ILES computation predict them well.

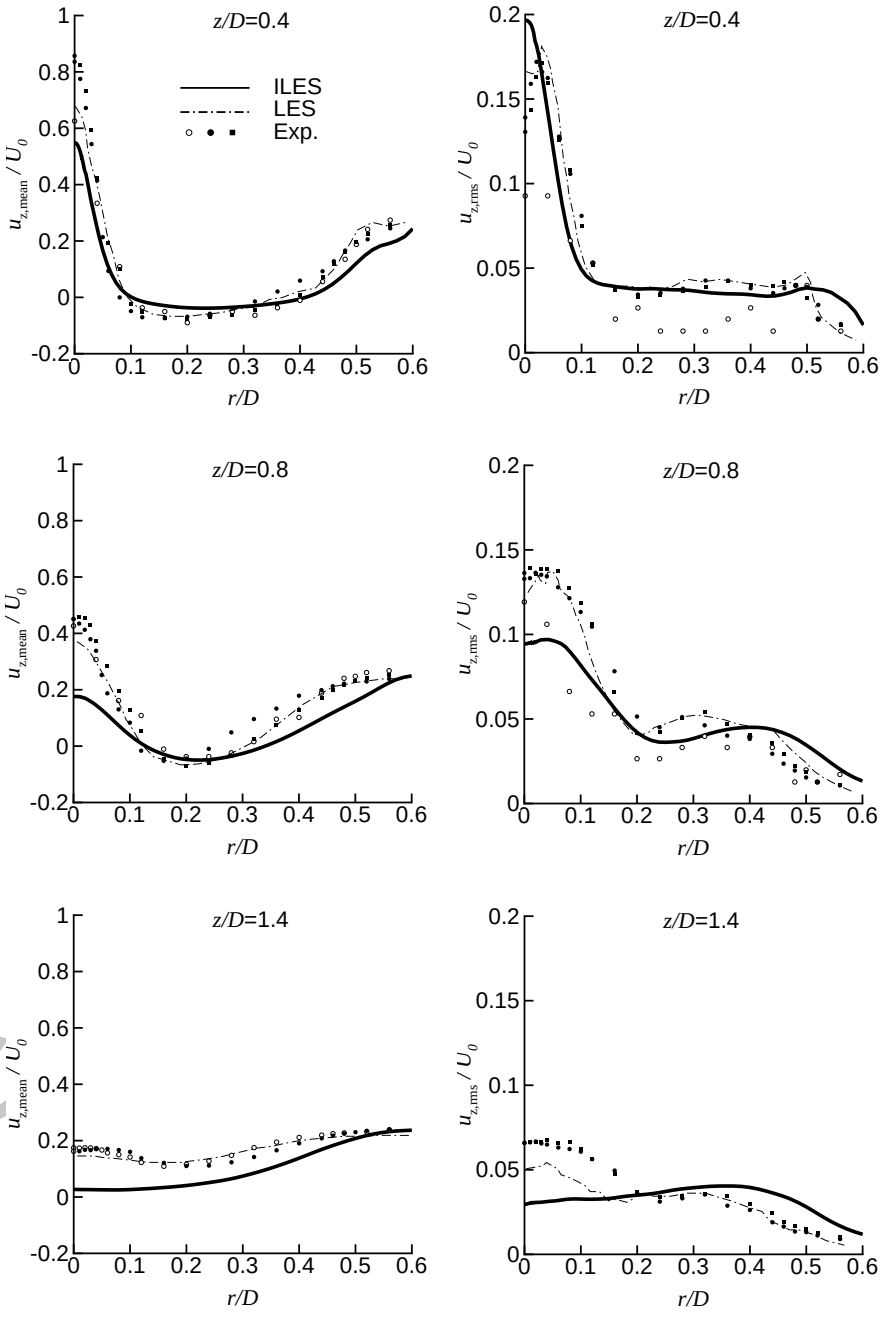

Figure 4: Mean axial velocity (left) and axial rms velocity (right) (fifth-order limiter, medium grid)

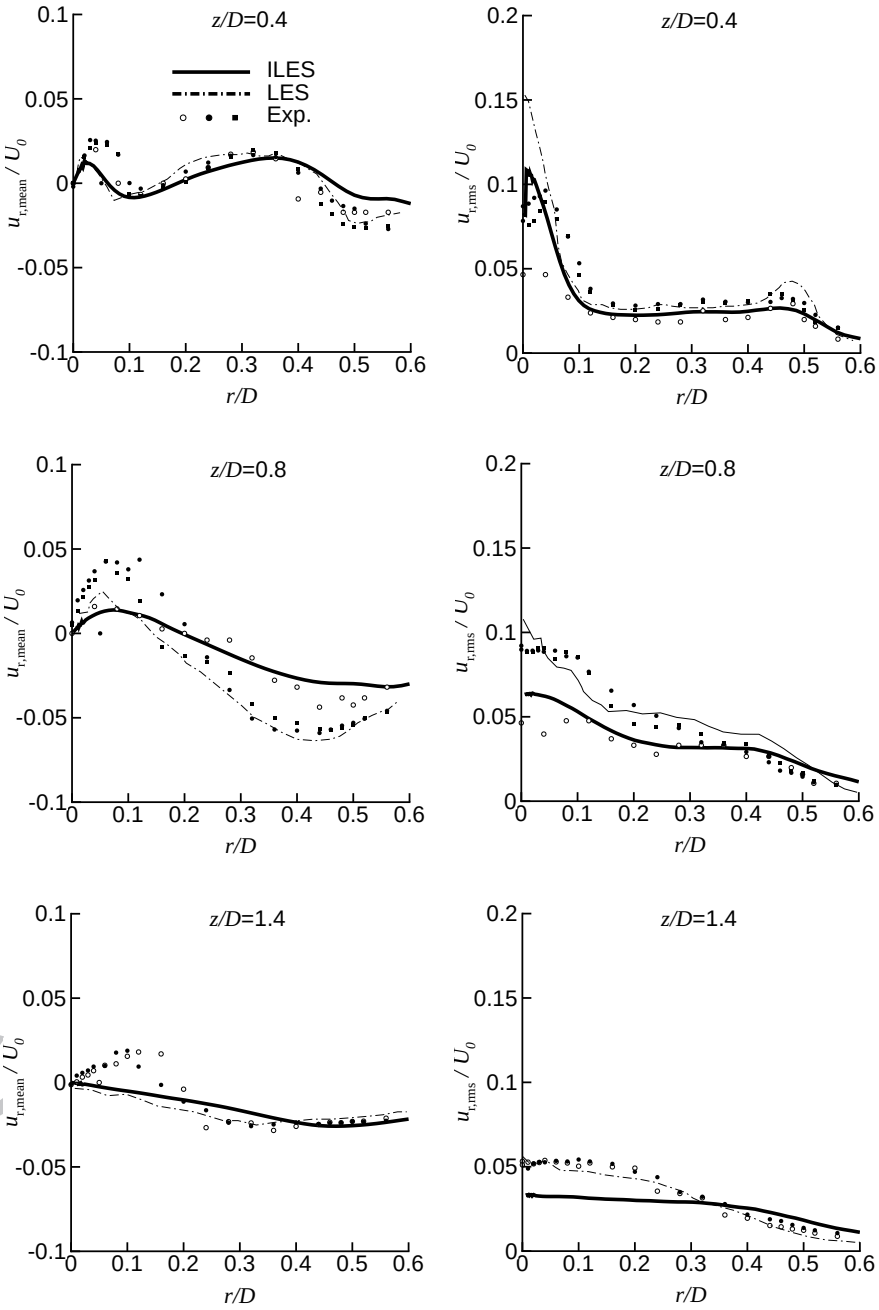

Figure 5: Mean radial velocity (left) and radial rms velocity (right) (fifth-order limiter, medium grid)

4.3. Multi-Species Mixing Field

The mixture fraction f is identical to the fuel mass fraction since no chemical reaction is considered and only two quiescent species, namely methane and air exist,

$$f = \frac{\alpha_f \rho_f}{\alpha_f \rho_f + \alpha_o \rho_o}. \tag{14}$$

Figure 6 shows the ILES results of mean mixture fraction and rms mixture fraction compared with experimental data [39]. Also, as described in the previous section, the large variance of the experimental data implies the sensitivity of the flow to the flow settings. By tracking volume fraction among quasi conservative equations, the ILES shows good agreement with experimental data.

4.4. Effects of Grid Resolution

Figure 7(left) shows the comparison of the mean axial velocity profile on the centreline ($r/D = 0.0$) for the different grid sizes. Note that all simulations in this sub-section were performed with the fifth-order accurate limiter. The medium and fine grid simulation show good convergence in $z/D < 0.6$ region and with maximum 3% difference in $z/D > 0.6$ region while the coarse grid result indicates maximum 8% deviation from the fine grid result. Figure 7(right) shows axial rms velocity of the same simulation. It clearly shows the advantage of the medium and fine grid. At $z/D = 0.4$ rms velocity is still larger than the experimental data which resulted in the deviation of the mean profile in the previous section. The effect of circumferential resolution was investigated by a grid having double points in the circumferential direction. The centreline velocity decayed faster compared to grids having normal points in the circumferential direction. The reason for this is is the large fluctuating velocity magnitude near the jet nozzle ($0.1 < z/D < 0.3$) as shown in the axial rms velocity graph.

The kinetic energy spectra were analysed to evaluate the performance of the implicit dissipation in the ILES approach by examining the behaviour of the resolved (unaffected by numerical dissipation) and unresolved scales (directly damped by numerical dissipation). The one dimensional kinetic energy spectrum $E(k, t)$ is defined as the square of the Fourier transform of the velocity,

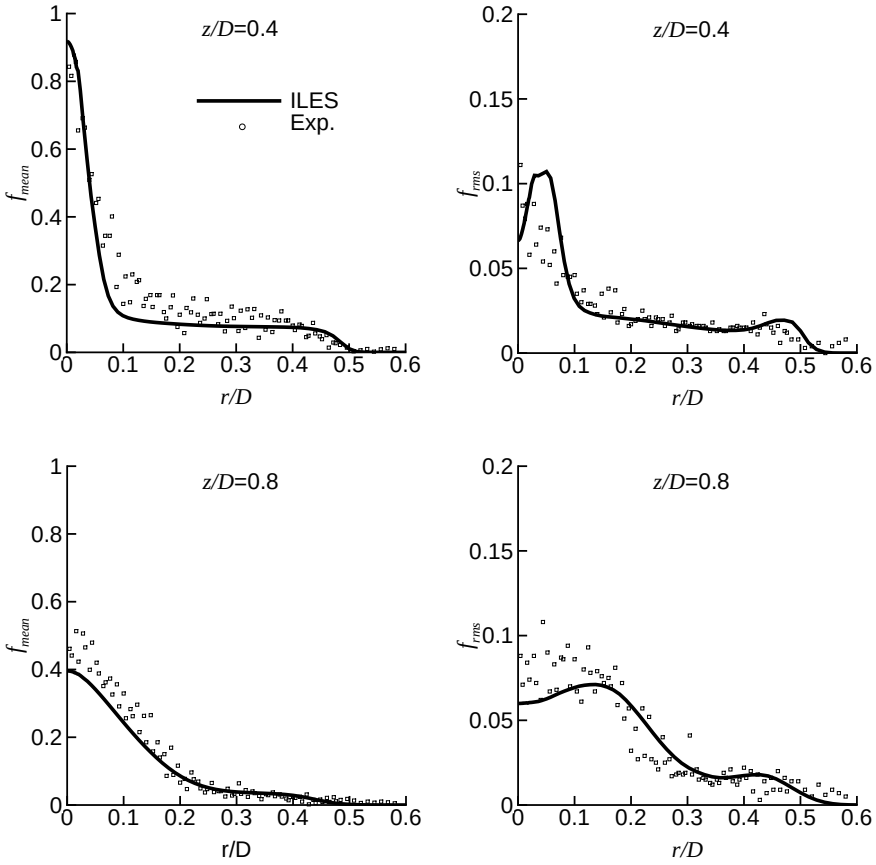

Figure 6: Mean (left) and rms (right) mixture fraction (fifth-order limiter, medium grid)

$$E(k,t) = \frac{1}{2\pi}\left|\int_{\infty}^{\infty} u(x_j,t) exp^{-Ikx_j} dx_j\right|^2, \tag{15}$$

where k and $u(x_j,t)$ denote wavenumber and velocity component in j direction, respectively. This was computed using the velocity time history at a selected spatial location with physical sampling period $114.8\,ms$ which corresponds to approximately 28 times passage of the fuel flow through the computational domain. Firstly, the fluctuating velocity field was examined to determine the appropriate spatial location to calculate the kinetic energy spectra. A region of strong turbulence can be seen at around $z/D = 0.4$ on the centreline in Figure 3(right) and hence, the point of $(r/D, z/D) = (0.0, 0.4)$

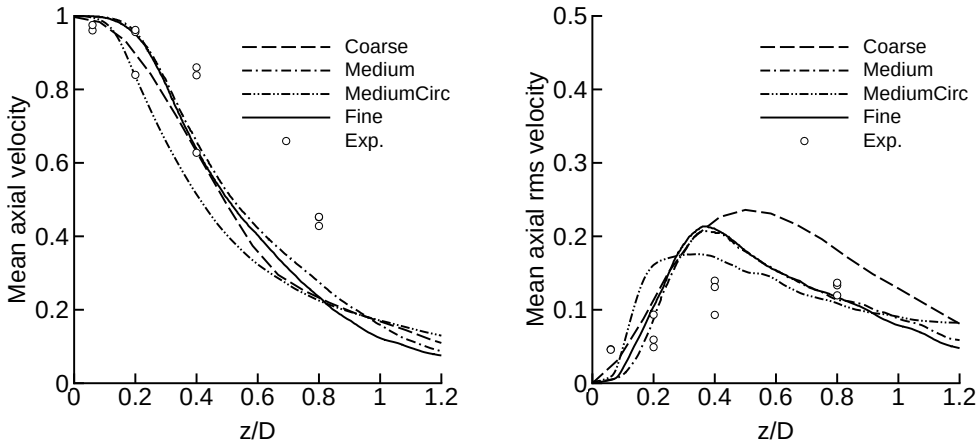

Figure 7: Mean axial velocity (left) and axial rms velocity (right) at $r/D = 0.0$ for different grid sizes (fifth-order limiter)

was selected. Then the kinetic energy spectra were calculated based on axial velocity components on the coarse, medium and fine grid. In Figure 8 the medium grid and fine grid results are almost identical demonstrating good convergence of the computation and grid independence. An inertial range in which the slope of the line is close to $k^{-5/3}$ [41] can be seen for all grids, particularly for the medium and fine grid. In the coarse grid, the 'cut-off'wavenumber k_{co} which describes the deviation point from $k^{-5/3}$ line is around 1.5×10^3. As the grid resolution increases the inertial range extends the cut-off wavenumber up to 2.0×10^4.

Finally, the maximum wavenumber k_{grid} produced by an instantaneous eddy rotation was estimated from the smallest possible eddy turnover time at a given grid. From the vorticity magnitude illustrated in Figure 2(right) the location of the eddies containing maximum vorticity is close to the centreline. With the assumption that the eddy containing maximum vorticity produces maximum velocity frequency, the corresponding k_{grid} are calculated. Table 2 shows that for all grid sizes the ratio of k_{grid} calculated above to the k_{co} are smaller than unity on the given grid, which means the ILES accounted for the energy transportation between large and small eddies appropriately.

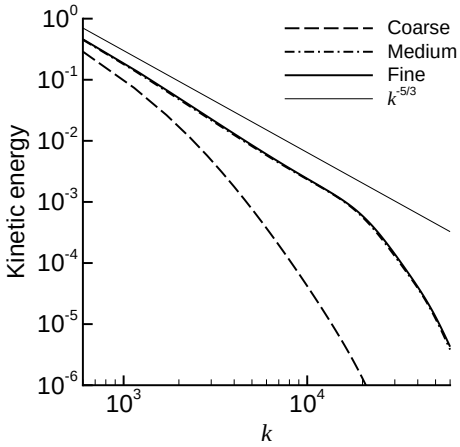

Figure 8: Kinetic energy spectra for different grid sizes (fifth-order limiter)

Grid	k_{co}	k_{grid}	k_{grid}/k_{co}
Coarse	1.50×10^3	1.10×10^3	0.73
Medium	1.50×10^4	5.15×10^3	0.34
Fine	1.50×10^4	5.37×10^3	0.36

Table 2: Effect of grid resolution on the effective cut-off wavenumbers

4.5. Influence of Order of Spatial Accuracy

Simulations with three different limiters which have second, fifth and ninth-order of accuracy, respectively, were carried out on the medium grid since the medium grid result in the previous sub-section showed good resolution of the kinetic energy with a smaller size grid and hence, smaller computational power than the fine grid. Figure 9(left) shows the influence of spatial accuracy of the limiters on the mean axial velocity profile on the centreline ($r/D = 0.0$). Three lines indicate only small differences, showing that a choice of the order of spatial accuracy higher than second order does not have significant effect on the temporally averaged velocity profile in this test case. Also, in Figure 9(right) axial rms velocity profiles of the same simulation illustrate small effects of the order of limiters.

Figure 10 shows the comparison of the kinetic energy spectra gained using each of these limiters, focusing on the region close to the effective cut-off. An

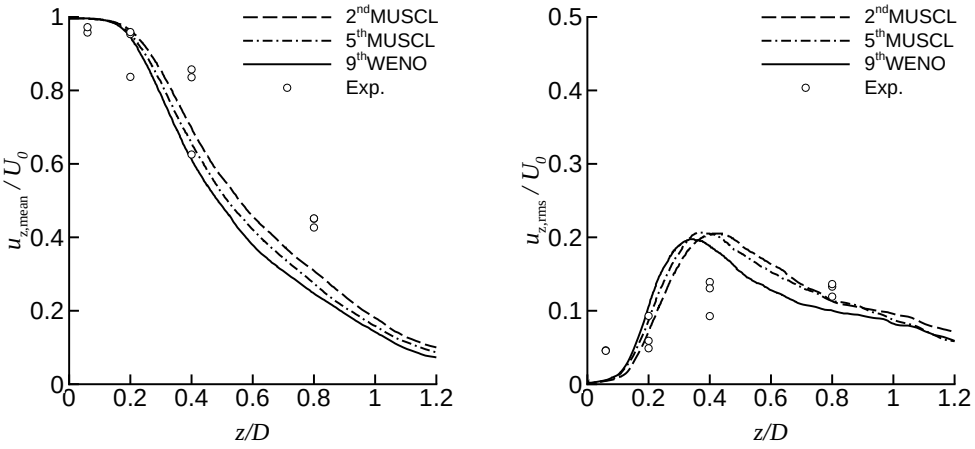

Figure 9: Mean axial velocity (left) and axial rms velocity (right) at $r/D = 0.0$ for different limiters (medium grid)

increase of the cut-off wavenumber can be seen as the order of accuracy of the limiter increases from second to fifth. However, the ninth-order limiter shows high kinetic energy in high wavenumbers ($2.0 \times 10^4 < k < 3.0 \times 10^4$) which implies that the numerical dissipation in this frequency range was smaller than ideal. As a result, the cut-off wavenumbers are close to the second and fifth order limiter.

Table 3 summarises the properties of the kinetic energy spectra for different limiters: k_{co}, k_{grid}, k_{grid}/k_{co} and a comparison of the required simulation time t_{sim} normalised by the time with the second-order limiter. The ratio k_{grid}/k_{co} are smaller than unity for all grid sizes. The fifth-order limiter showed a larger cut-off wavenumber and required only a slightly larger simulation time compared with the second-order limiter. With the ninth-order limiter the simulation demonstrated more than three times of the computational power was necessary compared with the second-order limiter.

5. Conclusions

An ILES technique based on high-resolution and high-order methods was used to investigate a turbulent mixing flow generated by a generic geometry injector. In the ILES simulation, the governing equations for compressible, single phase, multi-species, non reactive flow were solved without explicit modelling of the subgrid scales using a finite volume Godunov-type method.

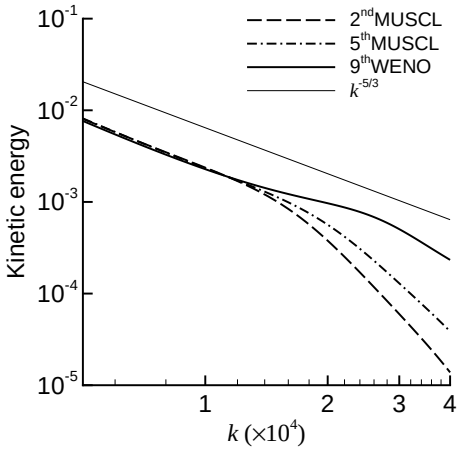

Figure 10: Kinetic energy spectra for three different orders of spatial accuracy (medium grid)

Limiter	k_{co}	k_{grid}	k_{grid}/k_{co}	t_{sim}
2^{nd} MUSCL	1.20×10^4	5.14×10^3	0.43	1
5^{th} MUSCL	1.50×10^4	5.15×10^3	0.34	1.08
9^{th} WENO	1.50×10^4	5.57×10^3	0.37	3.61

Table 3: Limiters effects on energy resolution and simulation time

Up to ninth-order spatial accuracy was used with a second-order explicit Runge-Kutta method for time integration.

Temporally and circumferentially averaged flow profiles were compared with the experimental data. The axial and the radial velocity and rms velocity profiles showed good agreement in the strong turbulent region, recirculation region and the downstream region of the flow fields. Also, the mixture fraction profiles demonstrated a good match to the experimental data in multi-species flow simulations.

The one dimensional kinetic energy spectrum was examined to evaluate the effects of grid resolution and limiter on energy dissipation in the ILES computation method. An ideal $k^{-5/3}$ decay of energy could be seen in a certain range which increased with grid resolution. In all computations with the fifth-order accurate limiter the cut-off wavenumbers are larger than

the estimated maximum wavenumbers appearing on the given computational grid. This implies that the numerical dissipation accounted for the energy transportation between large and small eddies sufficiently up to the effective cut-off.

The second, fifth and ninth-order limiter were examined on the medium grid. The fifth-order limiter showed good resolution of the kinetic energy dissipation with reasonable computational time compared to the second-order limiter. The ninth-order limiter required substantially larger computational power.

Acknowledgments

The authors would like to acknowledge technical support of the staff and the use of facilities at Cranfield's High Performance Computing facility.

References

[1] Barlow R, Dreizler A, Kempf A. Proceedings of the eighth international workshop on measurement and computation of turbulent nonpremixed flames, 2006.

[2] Barlow R, Dreizler A, Frank J, Janicka J, Kempf A, Lindstedt R, Masri A, Oefelein J, Pope S. Proceedings of the ninth international workshop on measurement and computation of turbulent nonpremixed flames, 2008.

[3] El-Asrag H, Menon S. Large eddy simulation of a swirling non-premixed flame. Proceedings of the 41st AIAA/ASME/SAE/ASEE joint propulsion conference 2005; AIAA-2005-3971.

[4] Ranga-Dinesh K, Kirkpatrick M. Study of jet precession, recirculation and vortex breakdown in turbulent swirling jets using LES. Comput Fluids 2009;38:1232-1242.

[5] Kempf A, Lindstedt R, Janicka J. Large-eddy simulation of a bluff-body stabilized nonpremixed flame. Combust Flame 2006;144:170-189.

[6] Kempf A, Malalasekera W, Ranga-Dinesh K, Stein O. Large eddy simulations of swirling non-premixed flames with flamelet models: A comparison of numerical methods. Flow Turbul Combust 2008;81:523-561.

[7] Germano M, Piomelli U, Moin P, Cabot W. A dynamic subgrid-scale eddy viscosity model. Phys Fluids A 1991;3(7):1760-1765.

[8] Pope S. Ten questions concerning the large-eddy simulation of turbulent flows. New J Phys 2004;6:35.

[9] Grinstein F, Margolin L, Rider W, ed. Implicit Large Eddy Simulation: Computing Turbulent Fluid Dynamics. Cambridge University Press, 2007.

[10] Margolin L, Rider W, Grinstein F. Modeling turbulent flow with implicit LES. J Turbul 2006;7:N15.

[11] Drikakis D. Advances in turbulent flow computations using high-resolution methods. Prog Aerosp Sci 2003;39:405-424.

[12] Drikakis D, Rider W. High-Resolution Methods for Incompressible Flows. Springer, 2005.

[13] Toro E. Riemann Solvers and Numerical Methods for Fluid Dynamics. Springer-Verlag, 1997.

[32] Drikakis D, Hahn M, Mosedale A, Thornber B. Large eddy simulation using high resolution and high order methods. Philos T Roy Soc A 2009;367:2985-2997.

[15] Fureby C, Grinstein F, Li G, Gutmark E. An experimental and computational study of a multi-swirl gas turbine combustor. Proc Combust Inst 2007;31:3107-3114.

[16] Grinstein F, Fureby C. LES studies of the flow in a swirl gas combustor. Proc Combust Inst 2004;30:1791-1798.

[17] Hahn M, Drikakis D. Implicit large-eddy simulation of swept wing flow using high-resolution methods. AIAA J 2009;47(3):618-629.

[18] Thornber B, Mosedale A, Drikakis D, Youngs D, Williams R. An improved reconstruction method for compressible flows with low Mach number features. J Comput Phys 2008;227:4873-4894.

[19] Youngs D. Numerical simulation of mixing by Rayleigh-Taylor and Richtmyer-Meshkov instabilities. Laser Part Beams 1994;12:725-750.

[20] Fureby C, Grinstein F. Large eddy simulation of high-Reynolds-number free and wall-bounded flows. J Comput Phys 2002;181:68-97.

[21] Drikakis D, Fureby C, Grinstein F, Youngs D. Simulation of transition and turbulence decay in the Taylor-Green vortex. J Turbul 2007;8:N20.

[22] Grinstein F. Recent progress on monotone integrated large eddy simulation of free jets. JSME Int J Ser B 2007;49(4):890-898.

[23] Margolin L, Smolarkiewicz P, Wyszogrodzki A. Implicit turbulence modelling for high Reynolds number flows. J Fluid Eng 2002;124:862-867.

[24] Dalziel S, Linden P, Youngs D. Self-similarity and internal structure of turbulence induced by Rayleigh-Taylor instability. J Fluid Mech 1999;399:1-48.

[25] Cohen R, Dannevik W, Dimits A, Eliason D, Mirin A, Zhou Y, Porter D, Woodward P. Three-dimensional simulation of a Richtmyer-Meshkov instability with a two-scale initial perturbation. Phys Fluids 2002;14(10):3692-3709.

[26] Smolarkiewicz P, Margolin L. MPDATA: a finite difference solver for geophysical flows. J Comput Phys 1998;140(2):459-480.

[27] Porter D, Woodward P, Pouquet A. Inertial range structures in decaying compressible turbulent flows. Phys Fluids 1998;10(1):237-245.

[28] Hickel S, Adams N, Domaradzki J. An adaptive local deconvolution method for implict LES. J Comput Phys 2006;213:413-436.

[29] Boris J, Grinstein F, Oran E, Kolbe R. New insights into large eddy simulation. Fluid Dyn Res 1992;10:199-228.

[30] Margolin L, Rider W. A rationale for implicit turbulence modeling. Int J Numer Meth Fl 2001;39,821-841.

[31] Thornber B, Drikakis D, Williams R, Youngs D. On entropy generation and dissipation of kinetic energy in high-resolution shock-capturing schemes. J Comput Phys 2008;227(10):4853-4872.

[32] Drikakis D, Hahn M, Mosedale A, Thornber B, Large Eddy Simulation Using High Resolution and High Order Methods Philosophical Transactions Royal Society A 2009, 367, 2985-2997.

[33] Allaire G, Clerc S, Kokh S. A five-equation model for the simulation of interfaces between compressible fluids. J Comput Phys 2002;181(2):577-616.

[34] Van Leer B. Towards the ultimate conservative difference scheme, IV: A new approach to numerical convection. J Comput Phys 1977;23(3):276-299.

[35] Kim K, Kim C. Accurate, efficient and monotonic numerical methods for multi-dimensional compressible flows: part II: multi-dimensional limiting process. J Comput Phys 2005;208(2):570-615.

[36] Balsara D, Shu C. Monotonicity preserving weighted essentially non-oscillatory schemes with increasingly high order of accuracy. J Comput Phys 2000;160(2):405-452.

[37] Hahn M, Drikakis D. Assessment of large eddy simulation of internal separated flow. J Fluid Eng 2009;131(7):071201.

[38] Dally B, Fletcher D, Masri A. Flow and mixing fields of turbulent bluff-body jets and flames. Combust Theor Model 1998;2:193-219.

[39] Masri A. Swirl flows and flames database. http://www.aeromech.usyd.edu.au/thermofluids/main_frame.htm accessed in May 2009.

[40] Kim J, Moin P, Moser R. Turbulence statistics in fully developed channel flow at low Reynolds number. J Fluid Mech 1987;177:133-166.

[41] Kolmogorov A. A refinement of previous hypotheses concerning the local structure of turbulence in a viscous incompressible fluid at high Reynolds number. J Fluid Mech 1962;13(1):82-85.